Electronic Supplement: Ascent rates of rhyolitic magma at the onset of three caldera-forming eruptions

Madison L. Myers[a,*], Paul J. Wallace[a], Colin J.N. Wilson[b], James M. Watkins[a], and Yang Liu[c]

[a] *Department of Earth Sciences, University of Oregon, Eugene, OR 97403-1272, USA*

[b] *School of Geography, Environment and Earth Sciences, Victoria University, PO Box 600, Wellington 6140, New Zealand*

[c]*Jet Propulsion Laboratory, California Institute of Technology, Pasadena, California 91109, USA.*

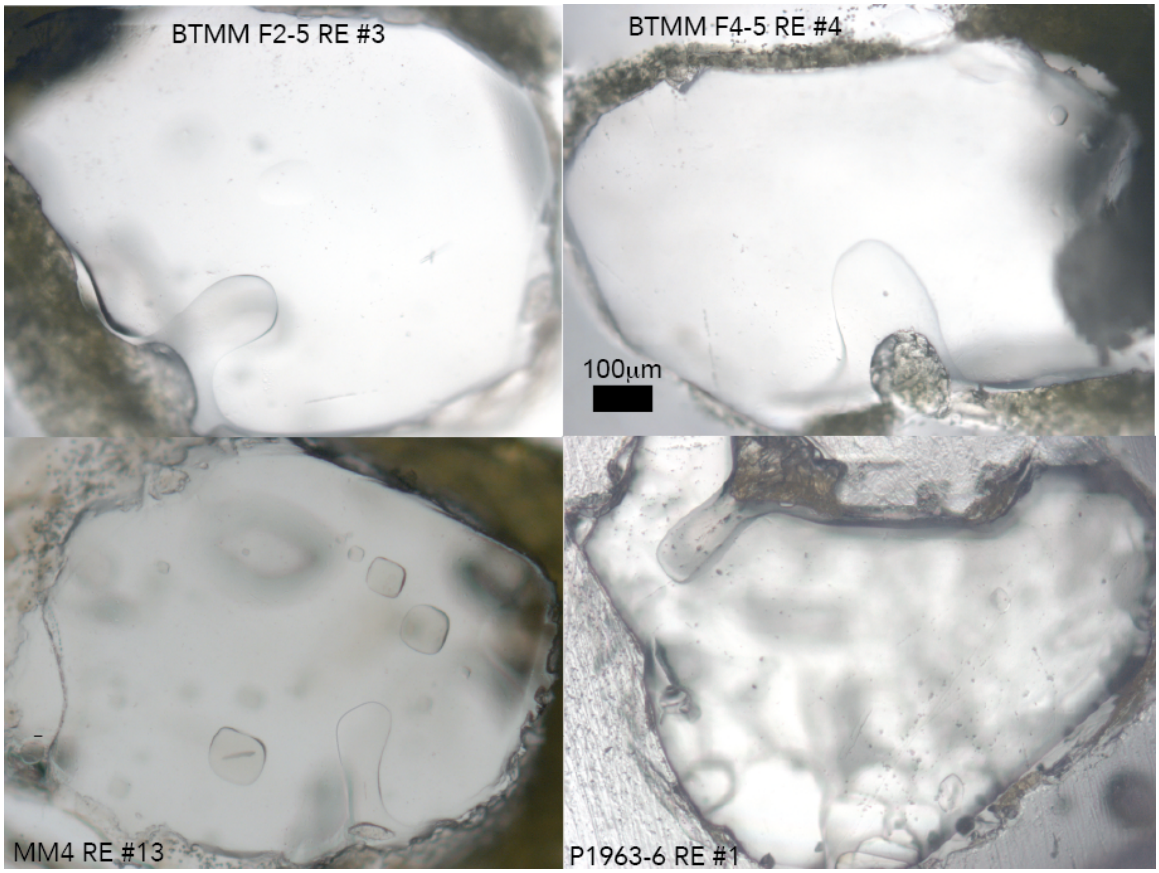

Supplement Figure 1: Photomicrographs of select reentrants that preserve well-formed bubbles at their mouths. Details on each reentrant can be found in Tables 1 and 2.

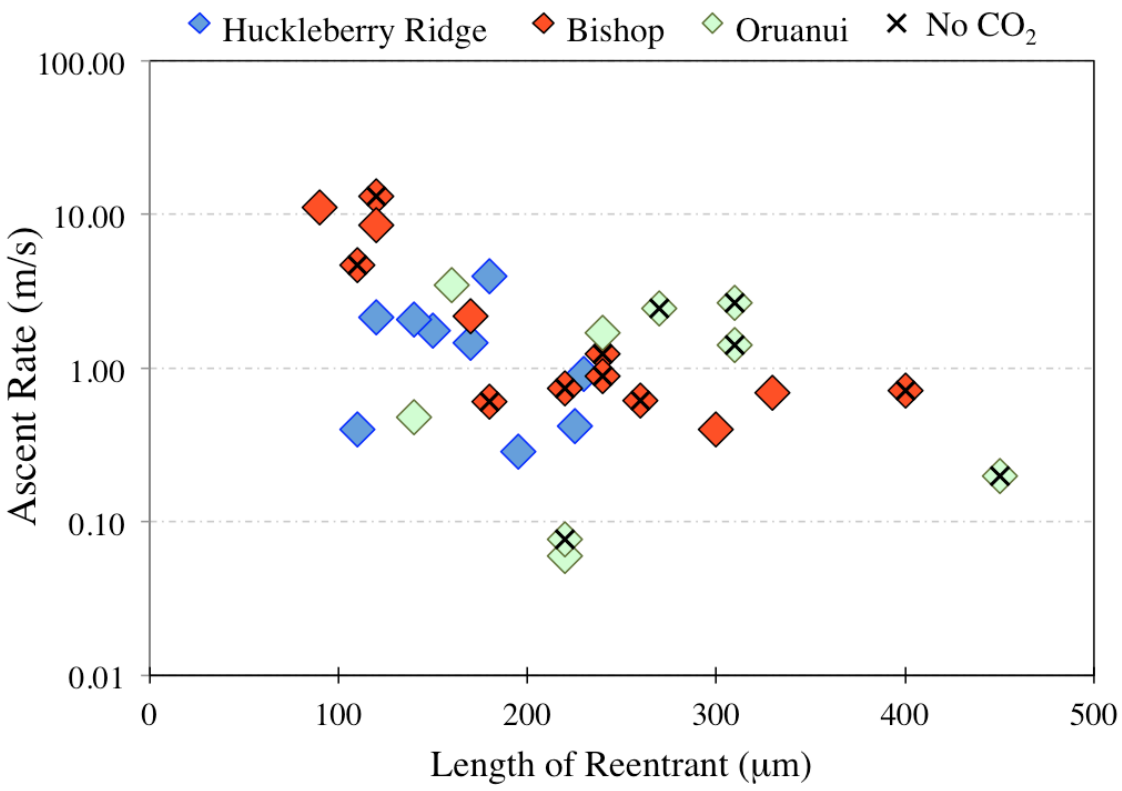

Supplement Figure 2: Ascent rate, in m/s, vs. the length of reentrant, in μm, for reentrants from all three eruptions. Although the fastest ascent rates are associated with the shortest reentrants, there is little correlation between ascent rate and length of reentrant.

Temperature Estimates

Here we discuss the constraints on the pre-eruption magmatic temperatures associated with the fall material for all three systems studied. In our reentrant diffusion modeling, we assumed that these temperatures remained constant during ascent, though we do separately consider how much calculated ascent rates would change if magma cooled by 20°C in the conduit (see Fig. 7). For all fall layers from the Bishop tuff we adopt a pre-eruptive temperature of 740 ºC (Hildreth, 1979, Bindeman and Valley, 2002; Hildreth and Wilson, 2007; Evans et al., 2016). Although in the later stages of the Bishop eruption there is evidence for an increase in magmatic temperature associated with the contribution of a less-evolved magma (Wark et al., 2007; Chamberlain et al., 2014), oxide pairs from the upper fall layers (units F7-F9) yield temperatures of 740 ºC (Hildreth and Wilson, 2007). Thus we have used this temperature for all modeling of Bishop reentrants. The temperature evolution of the pre-eruptive Oruanui magma body has been studied in great detail (Allan et al., 2013, 2017), constrained by Fe-Ti oxide, plagioclase-melt, orthopyroxene-melt, and amphibole-rim thermometry to yield a pre-eruptive estimate of 780±20 ºC (Allan et al., 2017). Temperature estimates for the Huckleberry Ridge fall deposit have been constrained to 800 ºC using Zr concentrations in melt inclusions and two-feldspar thermometry and through comparison with phase equilibrium relationships (Almeev et al., 2012; Myers et al., 2016).

Comparison between reentrant and melt inclusion starting conditions

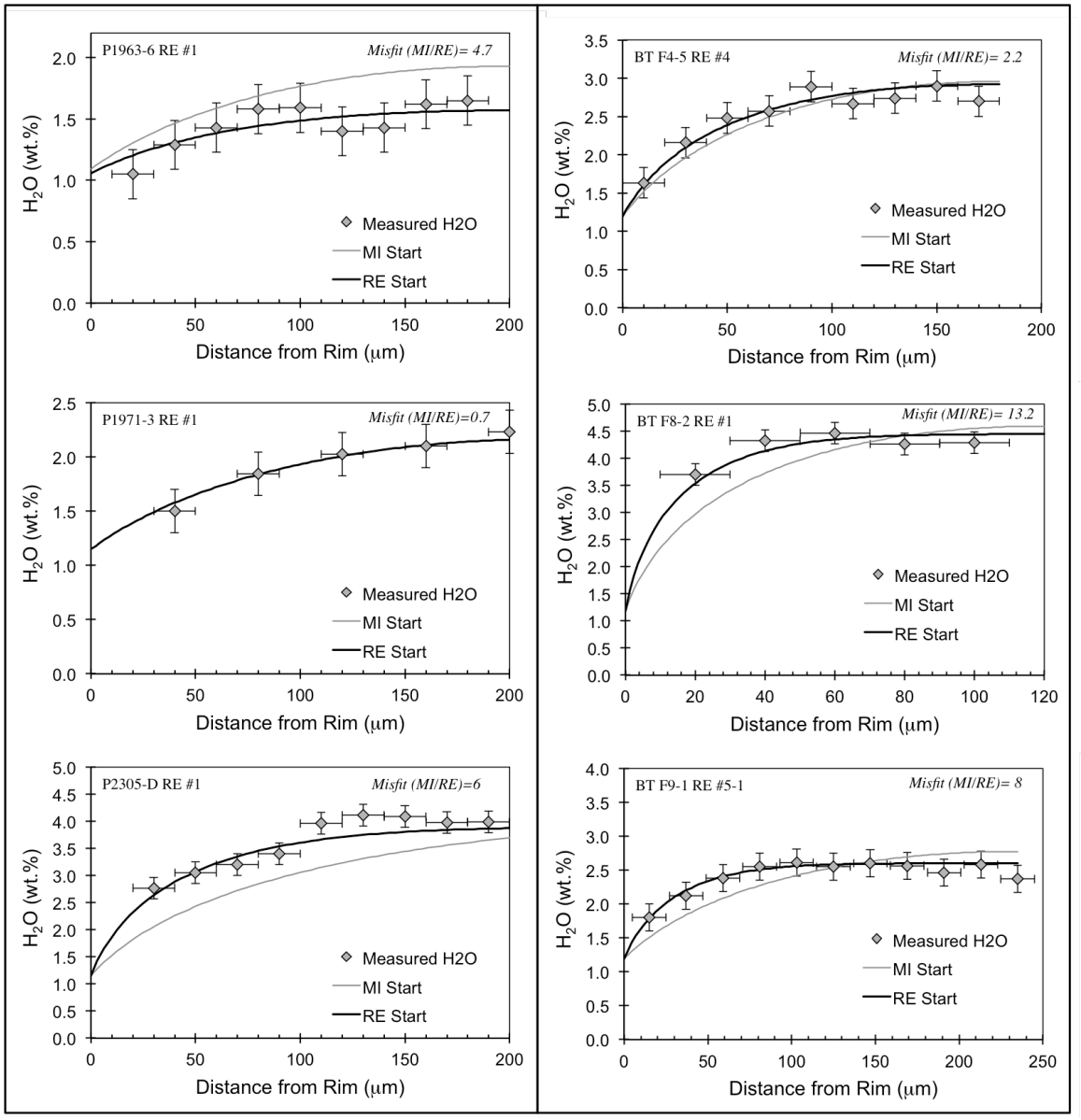

Supplement Figure 3: Select H_2O concentration profiles for three reentrants each from the Oruanui (left column) and Bishop (right column), where diamonds represent FTIR measured spots. All black solid lines represent the best fit profile using the interior reentrant concentrations as starting conditions, whereas gray lines are best fit profiles using a co-erupted melt inclusion for the starting concentrations. The misfit ratio (MI Chi^2/RE Chi^2) between using the melt inclusion vs. reentrant as starting conditions is given on each profile, where ratios range between ~1 (similar results) to 13 (reentrant starting conditions are far better). All Chi^2 profile fit values can be found in Table 3.

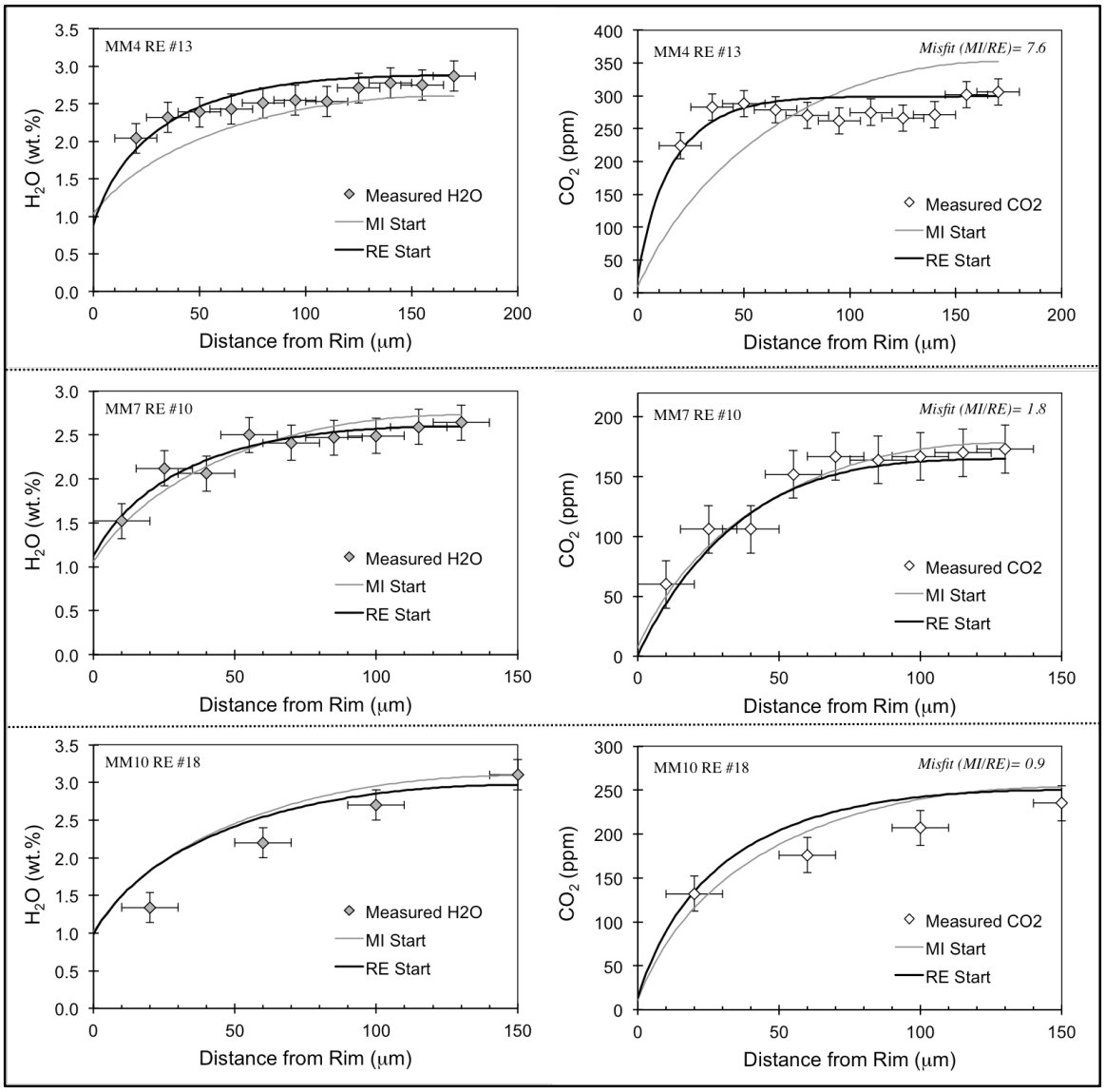

Supplement Figure 3 (continued): Select H_2O and CO_2 profiles for three reentrants from the Huckleberry Ridge Tuff; diamonds represent FTIR measured spots. All black solid lines represent the best fit profile using the interior reentrant concentrations as starting conditions, whereas gray lines are best fit profiles using a co-erupted melt inclusion for the starting concentrations. The misfit ratio (MI Chi^2/RE Chi^2) between using the melt inclusion vs. reentrant as starting conditions is given on the CO_2 profiles, where ratios range between ~1 (similar results) to 8 (reentrant starting conditions are far better). All Chi^2 profile fit values can be found in Table 3.

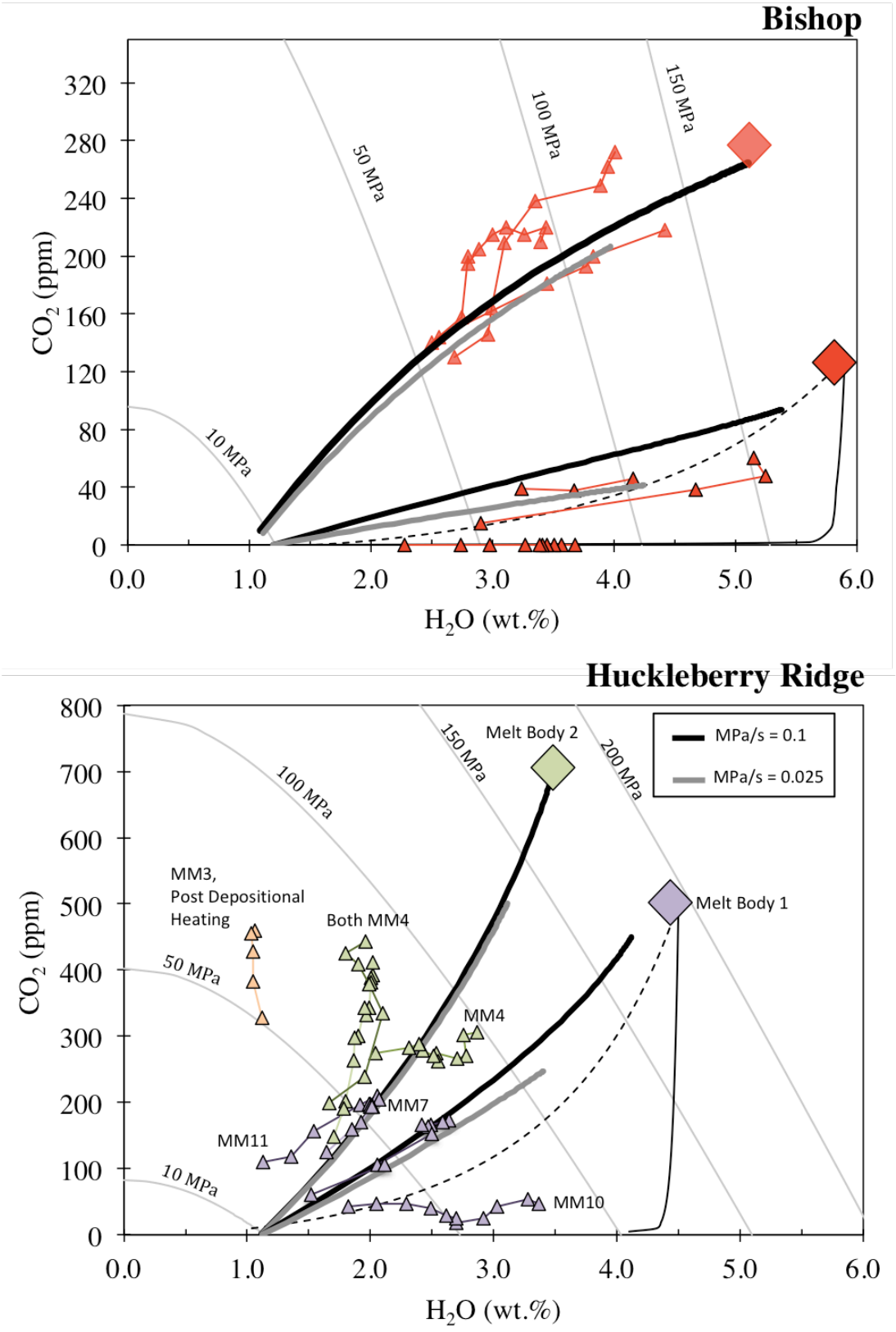

Supplement Figure 4:

Supplement Figure 4: (continued)

(Top) Comparison of RE profiles from the Bishop with H_2O-CO_2 vapor saturation curves and calculated degassing paths. Diamonds represent the two likely starting conditions determined from co-erupted quartz crystals (Wallace et al. 1999; Roberge et al. 2013; Myers 2017). Solid and dashed lines leading from 'F1-F9 MI Storage' represent open and closed system degassing, respectively, calculated using VolatileCalc (Newman and Lowenstern 2002). Thick black and gray lines from each starting location represent a theoretical RE profile that experienced either fast (0.1 MPa/s, black thick line) or slow (0.025 MPa/s, gray thick line) decompression. The decompression lines from the Ig1Ea start are modeled in the presence of an exsolved gas phase. Measured RE transects of H_2O and CO_2 are plotted as triangles.

(Bottom) Comparison of RE profiles from the Huckleberry Ridge with H_2O-CO_2 vapor saturation curves and calculated degassing paths. Diamonds represent the two likely starting conditions, determined from co-erupted Huckleberry MIs (Myers et al. 2016). Solid and dashed lines leading from 'Melt Body 1' represent open and closed system degassing, respectively, calculated using VolatileCalc (Newman and Lowenstern 2002). Thick black and gray lines from each 'Melt Body' represent a theoretical RE profile that experienced either fast (0.1 MPa/s, black thick line) or slow (0.025 MPa/s, gray thick line) decompression. Measured RE transects of H_2O and CO_2 are plotted as triangles. One RE from MM3 shows a near vertical profile. This layer is near the top of the fall layer, closer to hot, overlying ignimbrite. We interpret the flat H_2O profile of MM3 to be the result of post-depositional heating.

Comparison with Liu et al. (2007) decompression model

To validate our updated Matlab best-fit decompression script we ran two separate tests against the Liu et al. (2007) Fortran code. The first was to compare the profiles produced in both codes using the same starting conditions, decompression rate, and exsolved gas content for reentrants of different lengths (Supplement Figure 5). Agreement between the original 1-D Fortran code of Liu et al. (2007) and the one presented here is excellent, with the main difference being in the modeled CO_2 profiles. This is due to the use of an updated diffusion coefficient (faster) for CO_2 (Zhang et al. 2007) in our Matlab script, meaning that shorter reentrants and those that experienced slower decompression have larger offsets in the resulting modeled CO_2 profile (Supplement Figure 5).

Once we were confident that the codes were equivalent, we then tested the new 'best-fit' function, which cycles through a range of realistic decompression and exsolved gas contents, outputting those parameters that most closely produce a profile similar to a measured profile (lowest Chi^2 value). Test profiles were produced using the Liu et al. (2007) Fortran code from known starting concentrations, decompression rate, exsolved gas content, and reentrant length. The profile produced from each decompression run was then input as a RE profile in our Matlab script. The best-fit decompression rate and exsolved gas content given from our code to reproduce the Liu et al. (2007) profile was then compared to the values initially input in Liu et al. (2007). Agreement between the two decompression rates is excellent, and for all test runs decompression rates were within a factor of 1.2 (Supplement Table 3).

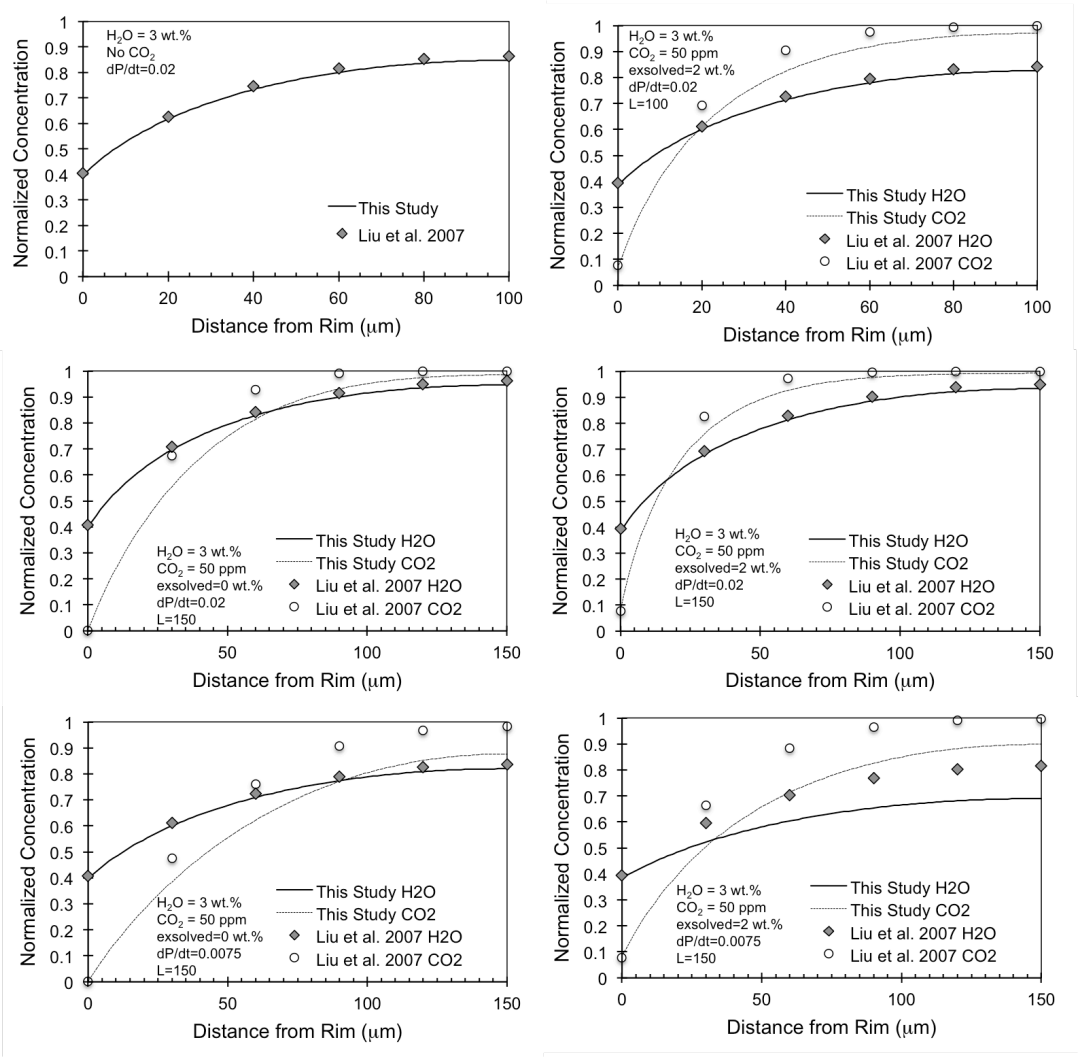

Supplement Figure 5: Comparison of modeled results from our code (shown as lines) with those using the Liu et al. (2007) code (data points) for various starting conditions. Important parameters that were tested in several model runs include: length of reentrant (μm), presence of an exsolve gas phase and decompression rate (MPa/s).

Modeling diffusive loss of H through quartz

The model used to calculate the amount of time associated with the extent of H diffusive loss from each MI through the quartz host assumes (for mathematical convenience) a spherical MI in the center of a spherical phenocryst (Qin et al., 1992; Cottrell et al., 2002). H diffusive loss is driven by the external melt having an H_2O concentration that is not in equilibrium with the H_2O concentration of the melt inclusion. As discussed in Myers et al. (2016), to calculate diffusive loss time during prolonged ascent, we need to constrain: (1) the diffusion coefficient of H in quartz, (2) the H_2O partition coefficient between quartz and the melt (0.0001*: Qin et al. 1992), (3) the initial MI H_2O concentration, and (4) the external H_2O concentration.

In Myers et al. (2016), a diffusion coefficient of 10^{-11} m^2/s was estimated, by fitting the H-loss experimental data of Severs et al. (2007). In Severs et al. (2007) heating of quartz-hosted Bishop MIs at 800 ºC and 1 kbar for various times (4 hrs to 63 days) showed that significant loss of H_2O from the MIs occurred within days. To calculate diffusion coefficients at the temperatures of relevance for the Oruanui (780ºC) and Bishop (740ºC) tuffs, we used the value at 800°C calculated using the data from Severs et al. (2007) and the Arrhenius relation $D = D_0\exp(-E/RT)$, where the activation energy E was taken from Kats et al. (1962). This gives a diffusion coefficient of 3.1×10^{-12} m^2/s for the Bishop, and 6.9×10^{-12} m^2/s for the Oruanui. The timescales calculated for H_2O loss from each MI are strongly dependent on the inclusion size and distance from crystal rim as input conditions (Lloyd et al., 2013). In all calculations we use the average inclusion diameter and the minimum distance to rim (measured in 2D section) as model parameters,

* This value was written incorrectly as 0.001 in Myers et al. (2016), but the correct value was used in all model runs presented in Myers et al. (2016).

providing a minimum timescale estimate (see Myers 2017 for all measurements and a full discussion).

To determine the initial H_2O concentration for each MI we assumed that H_2O behaved moderately incompatibly through partial loss to a vapor phase during vapor-saturated crystallization (see Myers et al. 2016 for Huckleberry Ridge, and Myers 2017 for Bishop and Oruanui reconstructions). For the external concentration we assumed that the MIs partially reequilibrated in external melts that had H_2O concentrations similar to the plateau values of H_2O found in the interiors of REs from the same sample.

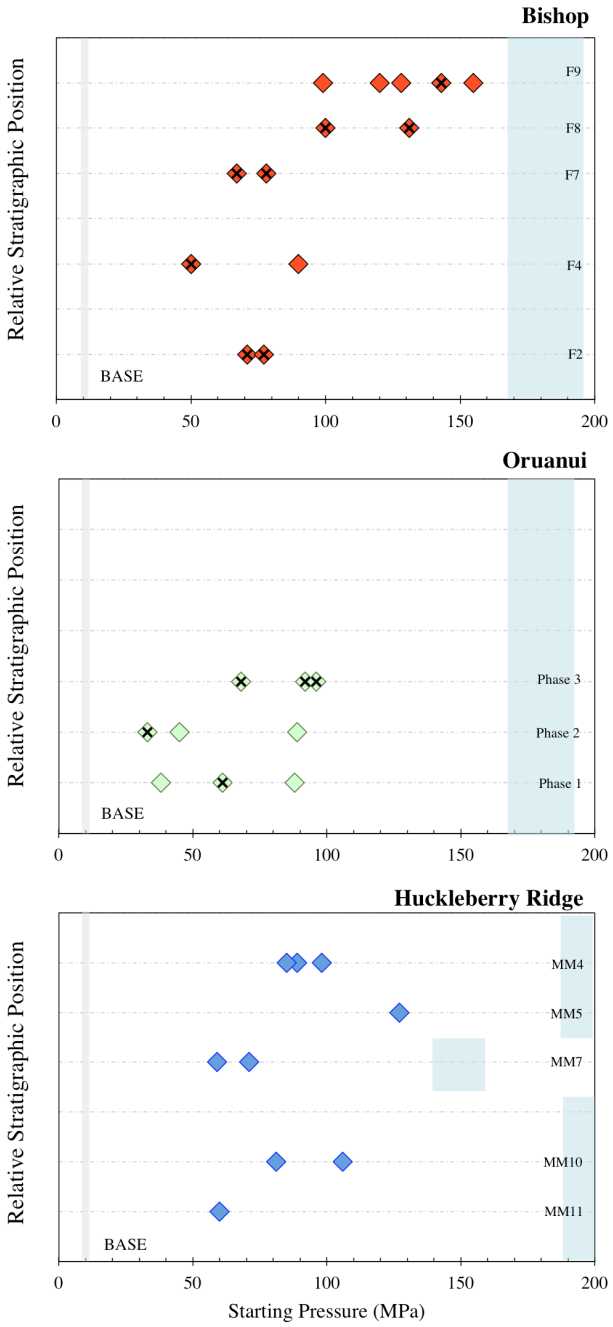

Supplement Figure 6: Summary of starting pressure estimates for each reentrant, based on the vapor saturation pressure associated with the innermost H_2O and CO_2 concentrations. Each reentrant is shown as a diamond; those containing X symbols contained no measurable CO_2. The gray line represents the fragmentation region used in this study. The blue region shows the range of pressures of magma storage based on data from co-erupted melt inclusions (Bishop: Wallace et al., 1999; Roberge et al., 2013; Huckleberry Ridge: Myers et al., 2016; Oruanui: Myers, 2017).

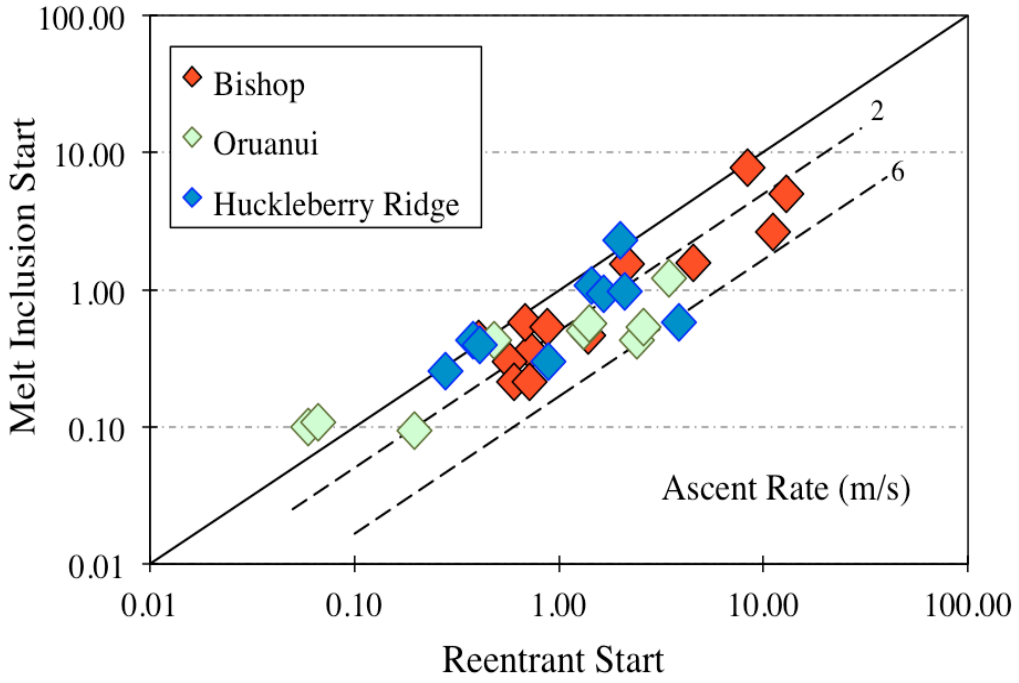

Supplement Figure 7: Comparison between the ascent rate (m/s) calculated using the melt inclusion concentration as the starting condition vs. using the concentrations of H_2O and CO_2 measured in the reentrant interior. Solid black line shows a 1:1 comparison; dashed lines show offset between the two starting conditions by factors of 2 and 6.

Supplement References

Allan, A.S., Morgan, D.J., Wilson, C.J.N., and Millet, M.A. (2013) From mush to eruption in centuries: assembly of the super-sized Oruanui magma body. Contributions to Mineralogy and Petrology, 166, 143-164.

Allan, A.S.R., Barker, S.J., Millet, M.-A., Morgan, D.J., Rooyakkers, S.J., Schipper, C.I., and Wilson, C.J.N. (2017) A cascade of magmatic events during the assembly and eruption of a super-sized magma body. Contributions to Mineralogy and Petrology, 172, 49.

Almeev, R.R., Bolte, T., Nash, B.P., Holtz, F., Erdmann, M., and Cathey, H.E. (2012) High-temperature, low-H_2O silicic magmas of the Yellowstone hotspot: an experimental study of rhyolite from the Bruneau–Jarbidge eruptive center, Central Snake River Plain, USA. Journal of Petrology, 53, 1837-1866.

Bindeman, I. N., & Valley, J. W. (2002). Oxygen isotope study of the Long Valley magma system, California: isotope thermometry and convection in large silicic magma bodies. Contributions to Mineralogy and Petrology, 144(2), 185-205.

Chamberlain, K.J., Morgan, D.J., and Wilson, C.J.N. (2014) Timescales of mixing and mobilisation in the Bishop Tuff magma body: perspectives from diffusion chronometry. Contributions to Mineralogy and Petrology, 168, 1-24.

Cottrell, E., Spiegelman, M., and Langmuir, C.H. (2002) Consequences of diffusive reequilibration for the interpretation of melt inclusions. Geochemistry, Geophysics, Geosystems, 3, 1026.

Evans, B.W., Hildreth, W., Bachmann, O., and Scaillet, B. (2016) In defense of magnetite-ilmenite thermometry in the Bishop Tuff and its implication for gradients in silicic magma reservoirs. American Mineralogist, 101, 407-414.

Hildreth, W. (1979) The Bishop Tuff: evidence for the origin of compositional zonation in silicic magma chambers. Geological Society of America Special Papers, *180*, 43-76.

Hildreth, W., and Wilson, C.J.N. (2007) Compositional zoning of the Bishop Tuff. Journal of Petrology, 48, 951-999.

Kats, A., Haven, Y., and Stevels, J. M. (1962) Hydroxyl groups in α-quartz. Physical Chemistry Glasses, *3*(3), 69-75.

Liu, Y., Anderson, A.T., and Wilson, C.J.N. (2007) Melt pockets in phenocrysts and decompression rates of silicic magmas before fragmentation. Journal of Geophysical Research, 112, B06204.

Lloyd, A.S., Ruprecht, P., Hauri, E.H., Rose, W., Gonnermann, H.M., and Plank, T. (2014) NanoSIMS results from olivine-hosted melt embayments: magma ascent rate during explosive basaltic eruptions. Journal of Volcanology and Geothermal Research, 283, 1-18.

Myers, M.L. (2017) Storage, ascent, and release of silicic magma in caldera-forming eruptions, 216 p. Ph.D. thesis, University of Oregon, Eugene.

Myers, M.L., Wallace, P.J., Wilson, C.J.N, Morter, B.J., and Swallow, E.J. (2016) Prolonged ascent and episodic venting of discrete magma batches at the onset of the Huckleberry Ridge supereruption, Yellowstone. Earth and Planetary Science Letters, 451, 285-297.

Newman, S., and Lowenstern, J.B. (2002) VolatileCalc: a silicate melt–H_2O–CO_2 solution model written in Visual Basic for Excel. Computers and Geosciences, 28, 597-604.

Qin, Z., Lu, F. and Anderson, A.T. (1992) Diffuse reequilibration of melt and fluid inclusions. American Mineralogist, 77, 565-576.

Roberge, J., Wallace, P.J., and Kent, A.J.R. (2013) Magmatic processes in the Bishop Tuff rhyolitic magma based on trace elements in melt inclusions and pumice matrix glass. Contributions to Mineralogy and Petrology, 165, 237-257.

Severs, M.J., Azbej, T., Thomas, J.B., Mandeville, C.W., and Bodnar, R.J. (2007) Experimental determination of H_2O loss from melt inclusions during laboratory heating: evidence from Raman spectroscopy. Chemical Geology, 237, 358-371.

Wallace, P. J., Anderson, A. T., and Davis, A. M. (1999) Gradients in H_2O, CO_2, and exsolved gas in a large-volume silicic magma system: Interpreting the record preserved in melt inclusions from the Bishop Tuff. Journal of Geophysical Research, 104, 20097-20122.

Wark, D.A., Hildreth, W., Spear, F.S., Cherniak, D.J., and Watson, E.B. (2007) Pre-eruption recharge of the Bishop magma system. Geology, 35, 235-238.

Zhang, Y., Xu, Z., Zhu, M., and Wang, H. (2007) Silicate melt properties and volcanic eruptions. Reviews of Geophysics, 45, RG4004.